CHEMISTRY
A European Journal

A Journal of
ChemPubSoc Europe

Accepted Article

Title: Prediction of EPR Spectra of Lyotropic Liquid Crystals using a combination of Molecular Dynamics simulations and the Model Free Approach

Authors: Vasily S. Oganesyan and Christopher Prior

To be cited as: *Chem. Eur. J.* 10.1002/chem.201702682

Link to VoR: http://dx.doi.org/10.1002/chem.201702682

Supported by
ACES

WILEY-VCH

10.1002/chem.201702682

WILEY-VCH

Prediction of EPR Spectra of Lyotropic Liquid Crystals using a combination of Molecular Dynamics simulations and the Model Free Approach

Christopher Prior[a] and Vasily S. Oganesyan [a]*

Abstract: We report the first application of fully atomistic molecular dynamics (MD) simulations to the prediction of the motional electron paramagnetic resonance (EPR) spectra of lyotropic liquid crystals in different aggregation states doped with a paramagnetic spin probe. The purpose of this study is twofold. First, given that EPR spectra are highly sensitive to the motions and order of the spin probes doped within lyotropic aggregates, simulation of EPR line shapes from the results of MD modelling provides an ultimate test bed for the force fields currently employed to model such systems. Second, the EPR line shapes are simulated using the motional parameters extracted from MD trajectories using the Model Free (MF) approach. Thus a combined MD-EPR methodology allowed us to test directly the validity of the application of the MF approach to systems with multi-component molecular motions. All-atom MD simulations using the General AMBER Force Field (GAFF) have been performed on sodium dodecyl sulfate (SDS) and dodecyltrimethylammonium chloride (DTAC) liquid crystals. The resulting MD trajectories were used to predict and interpret the EPR spectra of pre-micellar, micellar, rod and lamellar aggregates. The predicted EPR spectra demonstrate good agreement with most of experimental line shapes thus confirming the validity of both the force fields employed and the MF approach for the studied systems. At the same time simulation results confirm that GAFF tends to overestimate the packing and the order of the carbonyl chains of the surfactant molecules.

Introduction

Surfactant-water systems have been utilised by both nature (cell membranes) and humankind (e.g. detergents, lubricants, colloidal agents, drug delivery vectors) in a vast range of processes, and have been the subject of intense study for many years. Sodium dodecyl sulphate (SDS) and dodecyltrimethylammonium chloride (DTAC) (Figure 1), representing classical examples of anionic and cationic surfactants respectively, have been the target of a wide range of experimental techniques including nuclear magnetic resonance (NMR) [1, 2], electron paramagnetic resonance (EPR) [3-6], fluorescence [7], X-ray [8] and neutron scattering [9] as well as theoretical studies [10-14] in order to shed light on their structure and dynamics. Both systems are industrially ubiquitous, have well defined experimental phase diagrams exhibiting multiple lyotropic phases including micellar, rod/hexagonal and lamellar phases, as well as intermediate mixed structures [4, 15, 16] .

EPR with nitroxide spin probes has proven to be a particularly effective technique in the study of the dynamic behaviour of various soft matter systems [17-20] including lyotropic liquid crystals [3, 4, 6, 21] . EPR has the ability of directly resolving molecular reorientational dynamics on the sub-nanosecond time scale [22, 23]. Because of its high sensitivity only very low concentration of the probe is required (~100μM), so the host system is effectively unperturbed. Motional Continuous Wave (CW) EPR spectra provide two important pieces of information about partially disordered bulk states; firstly, local motions and order of molecules averaged over small volumes and, secondly, global (long-range) dynamics and order of the system that reflects on the geometry of the aggregate state. For instance, using the two-dynamic and disordered hexagonal models for fitting EPR spectra, Westlund and co-workers found that the local order parameter for the 5-DOXYL stearic acid (5DSA)

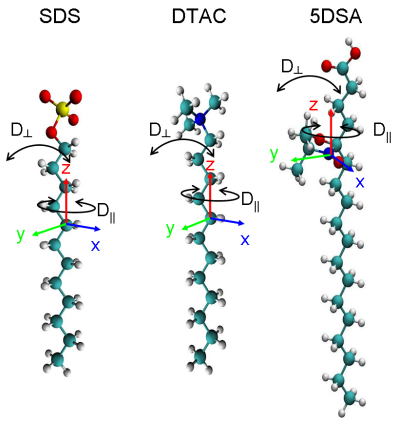

Figure 1. Structures of SDS, DTAC and 5DSA molecules with the molecular axes of surfactants SDS and DTAC and magnetic axes of 5DSA spin probe indicated. In 5DSA the X axis lies along N-O bond, Z axis is perpendicular to the nitroxide plane and Y axis is the vector product between the two. In host molecules the X axis lies along the C-H bond, Y axis is in the C-C-H plane and is perpendicular to X and Z is the vector product between the two.

doped within SDS/water systems was similar between micellar and aligned hexagonal samples at a given temperature, but that the hexagonal phase had slower dynamics [3]. Bahri et al. found

[a] C. Prior, Dr V. S. Oganesyan
School of Chemistry
University of East Anglia
Norwich, NR4 7TJ (UK)
E-mail: v.oganesyan@uea.ac.uk

Supporting information for this article is given via a link at the end of the document.

that both 5DSA and 16DSA spin probes result in similar EPR spectra when doped in SDS micelles [5]. Through the use of different buffer solutions they found EPR to be highly sensitive to micelle formation. Lindblom and co-workers reported a detailed analysis of the phase diagram of the DTAC/water system using EPR [4].

Although motional EPR line shapes are highly informative they require careful analysis in order to extract and differentiate between different motion and ordering contributions. Typically, simulation and fitting of EPR spectra are based on the solution of the Stochastic Liouville Equations (SLE) in the Fokker-Planck (FP) form (see computational methods) which was first applied to EPR by Freed and co-workers [24, 25], and is currently employed in a number of simulation suites [26, 27] . The adjustable parameters are the principle values of the rotational diffusion tensors of different motional contributions and the parameters that describe potentials that restrict these motions. Both sets of parameters can be related to the autocorrelation functions of reorientational dynamics of the three magnetic axes of the spin probe. In the case when two motional contributions, namely the internal restricted dynamics of the probe and the global dynamics of the environment, are well separated on the motional timescale, a useful simplification can be employed. Provided that the local motions of the probe are within the so-called motional narrowing limit ($\tau \leq 1$ ns), the magnetic tensors associated with the nitroxide head group can be partially averaged prior to the application of the SLE-FP procedure [28]. Global diffusion of an appropriate symmetry and restriction then leads to further averaging of the spectrum.

More rigorous augmented SLE methods such as the two dynamic and disordered hexagonal models used by Westlund and co-workers in the study of SDS aggregates [3] and the slowly relaxing local structure (SRLS) model developed by Freed's group [29] and applied commonly in the analysis of bulk partially disordered systems [30, 31], proteins[32, 33] and DNA [34], can be used to describe both motions. The principal difference between these two models is the inclusion of slippage of the probe in the SRLS model [29]. Because of the many parameters involved in describing the different motional contributions, multi-frequency EPR measurements are generally required and the fitting of EPR line shapes might not be unique [3, 34, 35]. In the case of hexagonal phases, an alternative is to use aligned samples in order to exploit their orientational anisotropy [3] .

An alternative framework used to interpret the diffusion of macromolecules is the Model-Free (MF) approach which aims to parameterise the time autocorrelation functions of molecular rotations without specific assumptions of the models mentioned above [36]. In particular the MF approach implies that the local and global motions are independent from each other in time. The approach has been used widely in the interpretation of NMR relaxation data [37-39]. More recently, it has been used to link the results of Molecular Dynamics (MD) simulations of proteins [40, 41] and lipids [42] with the NMR measurements. Although not as rigorous as the models mentioned above the MF approach is popular due to the ease of use and clarity of parameters estimated and interpreted.

The majority of previous MD simulation studies on lyotropic systems have been directed towards the geometry and thermodynamics of their aggregates [10-14] , with the predominant focus on the micellar phase. In the last decade novel approaches have been introduced that allow the prediction of motional EPR spectra from the generated MD data either indirectly [23, 43-45] or, more recently, by direct propagation of MD trajectories [23, 46-50]. Such techniques can greatly simplify the interpretation and analysis of experimental spectra, and hence provide unambiguous conclusions about molecular order and motions. These MD-EPR methods have been successfully applied to spin labelled proteins [43, 45, 47-49, 51, 52] and thermotropic liquid crystals [18, 53-57].

Here, a combined MD-EPR methodology is applied for the first time to various lyotropic aggregates. By employing the General AMBER Force Field (GAFF) we have performed extensive MD modelling of the main aggregates formed by SDS and DTAC doped with the 5DSA spin probe. GAFF has previously been shown to accurately reproduce structural properties of SDS micelles such as aggregate radii, eccentricity and counter ion binding as well as the lateral diffusion of carbon atoms in the alkyl chains [11, 14]. Geometric parameters such as aggregate radii and unit cell sizes are found to be in good agreement with previous experimental and theoretical studies. EPR spectral predictions for pre-micellar aggregates, micellar, rod and lamellar phases show good agreement with experiment. The application of the combined MD-EPR approach allows us to address two important questions at the same time. Firstly, by providing a direct link with experiment, it serves as a test bed for the force fields currently employed in the MD modelling of such systems. Secondly, the autocorrelation functions of molecular rotations can be readily generated from the resulting MD trajectories and subsequently fitted using the MF approach. The adjusted parameters, namely correlation times and order parameters, are then used to predict the motional EPR spectra and compare them to the experimental ones thus testing the validity of the widely used MF approach. Furthermore, by performing the MD analysis on the host liquid crystal molecules, the relationship between the motions of the host and the probe is explored.

Computational Methods

Parameterisation of 5DSA nitroxide spin probe - The GAFF parameters for 5DSA spin probe have been generated in analogy with other spin probes developed by us previously [51, 57]. Quantum chemical calculations of 5DSA were performed with the Gaussian 09 [58] software package, at the B3LYP/6-311++g(d,p) level of theory and the CHELPG [59] charge scheme to obtain partial charges. Force field parameters for the new atom types of the nitroxide moiety in 5DSA (the unsaturated carbon atoms of the nitroxide ring, the saturated carbon atoms of the nitroxide ring, the nitrogen and the oxygen) were taken from a combination of geometry optimization calculations in the gas phase and previous calculations [57]. Equilibrium bond

Table 1. System compositions and trajectory lengths

Phase	Number of water molecules	Number of surfactant molecules	Number of probe molecules	Trajectory length (ns)[a]
SDS Micro-Aggregates	6700	2-5	1	(10) 100
SDS Micelle	6300	58	2	(10) 300
DTAC Micelle	6100	40	2	(10) 300
SDS Hexagonal	2500	160	5	(20) 300
DTAC Hexagonal	1100	180	5	(20) 300
SDS Lamellar	2900	400	6	(30) 600
DTAC Lamellar	640	380	6	(30) 900

[a] Equilibration time is given in brackets

lengths and angles were taken directly from minimized energy structures. Force constants were interpolated using the reference values in the AMBER99 force field [60] and the quantum mechanical calculations of Barone and co-workers [61].

Details of MD modelling – Starting configurations for molecular dynamics were generated with the appropriate spherical, cylindrical or planar geometries using the DFT optimised molecular structures and Packmol software [62]. Multiple probes were dispersed in the larger aggregates in order to enhance the statistical accuracy and to improve the quality of the correlation functions (Table 1). MD simulations were performed with version 1.4 of the fully atomistic GAFF [63] supplemented with the additional parameters derived for 5DSA spin probe. The SPC/E water model [64] was used with the associated ion parameters developed by Cheatham and co-workers [65]. All calculations were performed with the AMBER 12 [66] MD package using an NPT ensemble with Ewald summation used to represent the long range Coulomb potential and periodic boundary conditions in all directions. A time step of 1 fs was used with output written to trajectory files every 20 ps. Temperature was maintained using a Langevin thermostat with a friction coefficient of 1 ps. A pressure of 1 atm with relaxation time of 2 ps was used and scaled appropriately for different phases. Simulations of micro-aggregate and micelle states doped with 5DSA were performed with isotropic pressure coupling. Hexagonal and lamellar phase simulations were performed with fully anisotropic pressure coupling. Micro-aggregate, micelle and hexagonal phase simulations were equilibrated for up to 30 ns. In the case of the lamellar phases, the structure was initially equilibrated with an applied surface tension (20 dyne/cm) for 15 ns, before a further 15 ns of equilibration without surface tension. Calculations employed a time step of 1fs, with production runs ranging from 100 to 900 ns (Table 1).

Autocorrelation functions and the MF analysis – The autocorrelation function of each vector, $\vec{l}$, associated with either the nitroxide head group of 5DSA or the host molecules as defined in Figure 1, can be calculated from an MD trajectory according to the following expression:

$$C(t) = \left\langle \int_0^\infty P_2(\vec{l}(\tau)) \cdot \vec{l}((t+\tau)) d\tau \right\rangle \quad (1)$$

where $P_2(x)$ is second order Legendre polynomial:

$$P_2(x) = \frac{1}{2}\left(3x^2 - 1\right) \quad (2)$$

and the bracket in (1) denotes the average taken over the orientation distribution, time and the number of available molecules. A sliding time window approach was used for time averaging [48]. In accordance with the MF approach, assuming that the global molecular motion is slower than the internal dynamics of the probe, $C(t)$ can be decomposed into the product of the correlation functions for the overall tumbling, $C^G(t)$ and the internal motion, $C^L(t)$.

$$C(t) = C^G(t)C^L(t) \quad (3)$$

Following the formalism introduced by Lipari and Szabo[36] and applying well known transformation properties of the Wigner rotational matrices one can derive the MF based expressions of the autocorrelation functions specific for the following states: micro-aggregate, spherical (micelle), cylindrical (rod/hexagonal) and bilayer (lamellae). They are provided in Supporting Information as equations S1, S2, S3 and S4 respectively, with the relationship between correlation times and the rotational diffusion tensor components given by equation S5. For example, in the simplest case of global isotropic rotation combined with the axially symmetric restrained internal motion, $C^G(t) = 1/5 \cdot \exp\left(-t/\tau^G\right)$ and $C^L(t) = S^2 + (1-S^2)\exp\left(-t/\tau^L\right)$ result in the following total normalised correlation function:

$$C(t) = \exp(-t/\tau^G)(S^2 + (1-S^2)\exp(-t/\tau^L)) \quad (4)$$

where S is the generalized order parameter of the internal motion and τ^G and τ^L are the correlation time for the global and local motions, respectively. The derived MF expressions were used to fit the autocorrelation curves to extract the order parameters and rotational correlation times for both local and global motions in all aggregate states. In each case the correlation function for the *Z* axis was fitted first. The resulting parameters were then fixed and the rest were obtained by fitting the X/Y correlation function.

Simulation of EPR spectra – The SLE:

$$\frac{\partial\rho(\Omega,t)}{\partial t} = -i\left[\hat{\hat{L}}(\Omega) + i\hat{\Gamma}\right]\rho(\Omega,t) \quad (5)$$

describes the time evolution of the density matrix, $\rho(\Omega,t)$, of the system [24, 67-69]. The states of the system are defined by general stochastic rotational coordinates, Ω, that evolve in space under the action of the stochastic generalized diffusional operator $\hat{\Gamma}$. The QM part of (5) is described by the Liouville superoperator $\hat{\hat{L}}(\Omega)$ of the spin Hamiltonian of the system which includes both the Zeeman and hyperfine interactions for the nitroxide probe:

$$\hat{H} = \beta\vec{\mathbf{B}}\mathbf{g}\hat{\mathbf{S}} + \hat{\mathbf{I}}\mathbf{A}\hat{\mathbf{S}} \quad (6)$$

According to Zerbetto et al. [70] the stochastic generalized diffusive operator can be presented in the following form:

$$\hat{\Gamma} = -\left(\frac{\partial}{\partial\Omega}\right)^T \mathbf{D}P_{eq}(\Omega)\left(\frac{\partial}{\partial\Omega}\right)P_{eq}^{-1}(\Omega) \quad (7)$$

expressed in terms of a diffusion tensor $\mathbf{D}$ and of $P_{eq}(\Omega)$, the equilibrium Boltzmann distribution defined with respect to the total energy of the system and satisfying the condition $\hat{\Gamma}P_{eq} = 0$. In the case of a single rotational diffusion contribution, and in the absence of restricted potentials, the operator $\hat{\Gamma}$ reduces to the following well known form:

$$\hat{\Gamma} = D_{XX}\hat{J}_X^2 + D_{YY}\hat{J}_Y^2 + D_{ZZ}\hat{J}_Z^2 \quad (8)$$

where D_{ii} are the principle values of the rotational diffusion tensor describing this motion and $\hat{J}_i$ are the components of the angular momentum operator. $P_{eq}(\Omega)$ in (7) is predetermined by the probe's ordering potentials [70]. In many cases the restriction of the motion can be well approximated by the axially symmetric potential in the Maier-Saupe form, namely, $V(\theta) = -\varepsilon(3\cos(\theta)^2 - 1)/2$ **,** where θ represents the azimuthal angle of the potential**.** The strength of the potential ε can be readily worked out from the order parameter S using an integrated numerical dependence [27].

EPR spectrum is then obtained as the Fourier-Laplace transform of the SLE:

$$I(\omega-\omega_0) = 1/\pi\,\mathrm{Re}\left\langle u\left\|\left(i(\omega-\omega_0) + i\hat{\hat{L}} + \hat{\Gamma}\right)^{-1}\right|uP_{eq}\right\rangle \quad (9)$$

where ω and ω_0 are the sweep and Larmour frequencies, respectively, and $|u\rangle$ defines the QM spin transition states in the Liouville space [24, 68, 70].

The simulation of motional EPR line shapes can be simplified by taking into account the fact that for many surfactant/water systems the internal reorientational dynamics of the probe is usually very fast ($D > 10^8$ s^{-1}) on the EPR timescale at X-Band (~ 9.5 GHz) [3]. In such cases the effects of fast local motions can be accounted for prior to solving the SLE by partial averaging of the magnetic parameters in response to the local axial order, represented by order parameter S^L, in accordance with the equations (10) derived by Gaffney and McConnell [71]:

$$\begin{aligned}
\bar{g}_\perp &= g_0 - \frac{1}{3}S^L\left(g_{zz} - \frac{1}{2}(g_{xx}+g_{yy})\right)\\
\bar{g}_\parallel &= g_0 + \frac{2}{3}S^L\left(g_{zz} - \frac{1}{2}(g_{xx}+g_{yy})\right)\\
\bar{A}_\perp &= A_0 - \frac{1}{3}S^L\left(A_{zz} - \frac{1}{2}(A_{xx}+A_{yy})\right)\\
\bar{A}_\parallel &= A_0 + \frac{2}{3}S^L\left(A_{zz} - \frac{1}{2}(A_{xx}+A_{yy})\right)
\end{aligned} \quad (10)$$

where $\bar{g}_\perp$, $\bar{g}_\parallel$, $\bar{A}_\perp$ and $\bar{A}_\parallel$ are the partially averaged principle components of ***g*** and ***A*** tensors and $g_0 = (g_{xx}+g_{yy}+g_{zz})/3$ and $A_0 = (A_{xx}+A_{yy}+A_{zz})/3$.

The averaged values are then employed in the SLE simulation algorithm with the $\hat{\Gamma}$ operator now depending only on global diffusion parameters. The principle values of the ***g*** and ***A*** tensors used in this study were: g_{xx} = 2.0088 ; g_{yy} = 2.0061 ; g_{zz} = 2.0027 and A_{xx} = 6.26 G ; A_{yy} = 5.85 G ; A_{zz} = 33.46 G, respectively [71]. EPR spectra were simulated using the Easyspin package [26] . The values of homogeneous line broadening used in EPR simulations are detailed in Table S1 of SI [3, 4].

Global diffusion which depends on the geometry of the aggregate further averages the spectra, as illustrated with the selected model simulations in Figure 2. For instance, in spheroidal micelles, global motions due to surface diffusion of the probe and aggregate tumbling totally average out the anisotropy of the local motions resulting in significant narrowing of the line shapes (Figure 2a) [3]. On the other hand, in the highly anisotropic cylindrical aggregations of the hexagonal phase,

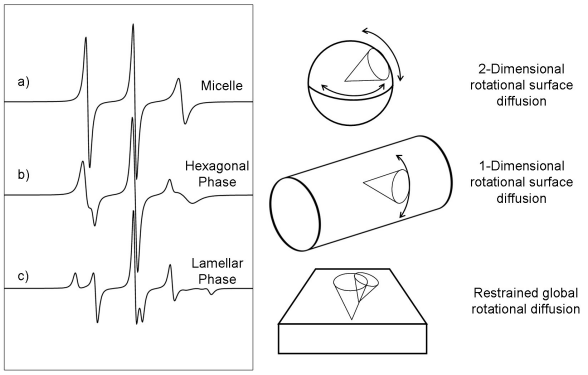

Figure 2. Left: Illustrative examples of X-band EPR line shapes simulated using partial averaging of magnetic parameters of a spin probe with restricted local motion (S^L = 0.4) and combined with: **a)** two dimensional surface diffusion (micelle) ($D_\perp^G$ = 5 × 10^7 s^{-1}); **b)** one dimensional surface diffusion (rod/hexagonal phase - unaligned) ($D_\perp^G$ = 5 × 10^7 s^{-1}); **c)** restrained global rotational diffusion (S^G = 0.2) near the rigid limit (lamellar) ($D_\perp^G$ ~ 1 × 10^6 s^{-1}). Right: Diagram showing ordered local motions (cones) and rotational global motions (arrows) in different aggregates.

there is only one-dimensional surface diffusion which is far less effective at averaging out the anisotropy of the local motion, leading to an intermediate powder spectrum (Figure 2b). In the lamellar phase, surface diffusion in both directions is assumed to be mainly translational with no effect on the line shape, resulting in significantly broader line shapes that depend sensitively on the S^L value of the internal motion of the probe (Figure 2c). A slow restrained motion as a result of ripples on the surface of the lamellae or other tilting motions may exist and affect the dynamics of the probe [72]. However, as long as such motions are very slow on the EPR time scale ($D < 10^6$ s^{-1}), their effect on the relevant line shapes becomes negligible. In such a case the microscopic order macroscopic disorder (MOMD) [73] simulation model can be readily applied considering only the internal dynamics of the probe.

Experimental Methods

Sample preparation is described in Section 1 of Supporting Information (SI). EPR spectra were measured using an X-band (9.5 GHz) Bruker EMX spectrometer equipped with the digital temperature control system (ER4131VT) for high temperature measurements using a heated flow of nitrogen gas. For each temperature, samples were equilibrated for 5 minutes before taking the measurement. Variable temperature measurements were performed with the tolerance < 0.1 K. The following conditions were used: microwave frequency of 9.55 GHz; microwave power of 2 mW; modulation frequency of 100 kHz; modulation amplitude of 1.0 G.

Results and Discussion

Lyotropic micro-aggregates – Micro-aggregate states of lyotropics have been modelled using SDS molecules. Previous experimental studies have suggested that due to the hydrophobic nature of the 5DSA spin probe, limited aggregation centred around the probe can occur below the critical micelle concentration [74].

By starting MD simulations with a random dispersion of up to five SDS molecules and one probe in a simulation box filled with water molecules, the formation of flexible micro-aggregates around the spin probe was observed in < 10 ns (Figure 3a). In fact, SDS molecules did not form stable micro-aggregates except in the presence of 5DSA. It was also observed that the larger micro-aggregates (with either 4 or 5 SDS molecules) were more stable, however infrequent reversible dissociation of SDS molecules still took place.

Autocorrelation functions calculated from the MD trajectory for different molecule fixed axes in both probe and host molecules, corresponding to a micro-aggregate with 3 SDS molecules, are shown in Figure 3b. They were fitted using the relevant expression S1 from SI, along with other micro-aggregates, and the results are presented in Table 2 (For all systems reported in this paper the fitted curves are presented in SI). The dynamics in

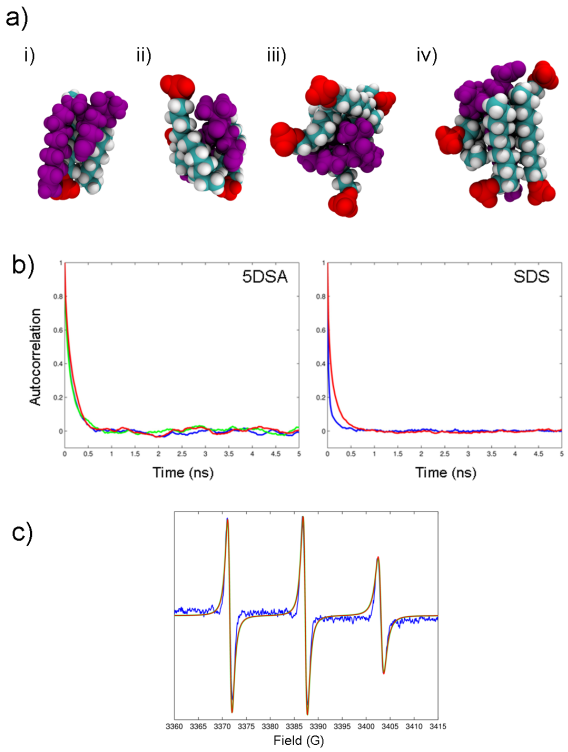

Figure 3. a) Snapshots of 5DSA spin probe (purple) in SDS micro-aggregates consisting of 2 (i), 3 (ii), 4 (iii) 5 (iv) surfactant molecules. In all images water molecules are excluded for clarity. **b)** Left: Rotational autocorrelation functions of the magnetic axes *X* (blue), *Y* (green) and *Z* (red) of the 5DSA spin probe in 3 SDS pre-micellar micro-aggregate at 300K; Right: Rotational autocorrelation functions of *X, Y* (blue) and *Z* (red) molecular axes of SDS surfactants in micro-aggregate. The axes for both the probe and the host molecules are shown in Figure 1. **c)** Comparison between experimental (blue) and simulated (red) EPR spectra of 5DSA assuming discrete Gaussian distribution among micro-aggregates at 300K. The green line represents the EPR spectrum of a single 3 SDS micro-aggregate at 300K.

all micro-aggregates were found to have slight axial rotational character, reflecting the rod like molecular geometry of both the individual molecules and their aggregates. This was particularly noticeable for SDS molecules with the clearly distinguishable correlation decays for the *Z* and *X/Y* axes (Figure 3b, right panel). Larger aggregates exhibited slower dynamics (Table 2) as a result of the greater size and less frequent dissociation of surfactant molecules. In all cases, the rotational dynamics of the nitroxide group on the probe were slower than that of the host SDS backbone. The EPR spectrum of micro-aggregates with 3 SDS molecules predicted using the MF approach is shown in Figure 3c as the green line and is in excellent agreement with the experimental one (blue line) measured at 3mM SDS concentration. A distribution of aggregate sizes would be expected in an experimental sample. The spectrum averaged among the simulated aggregate contributions assuming a narrow discrete Gaussian distribution around 3 SDS aggregate with the variance $\sigma^2 = 0.25$ is shown as the red line. It is barely

Table 2. Motional parameters of 5DSA and SDS in different micro-aggregate states at 300K obtained from the fitting of the relevant autocorrelation functions.

	$D_{\perp}$ (s^{-1})	$D_{\parallel}$ (s^{-1}) [a]
	2 SDS molecules	
5DSA	12.67×10^{8}	2.73×10^{9}
SDS	17.60×10^{8}	2.01×10^{10}
	3 SDS molecules	
5DSA	10.75×10^{8}	2.11×10^{9}
SDS	15.26×10^{8}	1.84×10^{10}
	4 SDS molecules	
5DSA	7.45×10^{8}	1.79×10^{9}
SDS	9.73×10^{8}	1.80×10^{10}
	5 SDS molecules	
5DSA	6.39×10^{8}	1.57×10^{9}
SDS	9.27×10^{8}	1.75×10^{10}

[a] $D_{\perp}$ and $D_{\parallel}$ represent the two components of a single axial rotational diffusion employed in the model for all micro-aggregates. 95% confidence bounds for the adjusted parameters are provided in Table S2 of the SI.

distinguishable from the one corresponding to 3 SDS micro-aggregate.

Micelle – Figure 4a shows the equilibrated structures of 5DSA (purple) doped in SDS (left) and DTAC (right) micelles composed of 60 (N60) [6, 10, 13, 14] and 40 (N40) [4, 12] molecules respectively at 320K. The structures clearly highlight the differences in packing between the two surfactant systems. Due to the larger size, many of the alkyl chains in the SDS micelle are solvent exposed. This results in significantly greater geometric disorder compared to the DTAC micelle as the tails fold to minimise contact with water in the former.

This behaviour has been observed in previous MD studies of SDS micelles [10], as well as inferred by experimental studies that found that changing from the 5DSA probe to 16DSA had little effect on their EPR spectra, indicating that tail and head experienced similar environments [5]. In contrast, in the slightly smaller DTAC micelle, even though a similar bent conformation is observed, the tails tend to remain directed towards the micelle centre. The SDS micelle was found to be stable over the entire MD trajectory at three selected temperatures, in agreement with the previous MD study by Jang and co-workers which reported that external energy of ~13 kcal/mol was required for the dissociation of the SDS molecules [10]. Conversely, our results show that in the DTAC micelle individual molecules temporarily

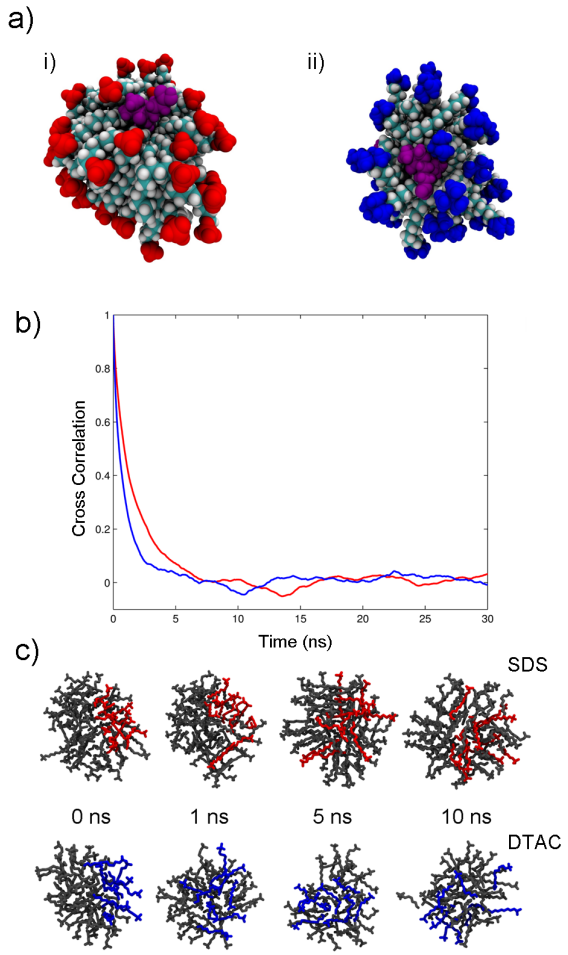

Figure 4. a) Equilibrated structure of N60 SDS (left) and N40 DTAC (right) micelles at 320K doped with 5DSA spin probe (purple). In all images water molecules are excluded for clarity. **b)** Cross-correlations of SDS (red) and DTAC (blue) molecular *Z* axes in micelle at 320K. **c)** Snapshots of SDS and DTAC micelles showing the effect of surface diffusion using a selection of molecules shown in red and blue for SDS and DTAC respectively.

dissociate spontaneously, albeit infrequently. This process contributes to the greater fluctuations in the micelle radii and eccentricity for the DTAC micelle compared to SDS whose time evolutions are presented in Figure S1 of SI. For instance, the radii, defined as micelle centre of mass (COM) to Sulphur, of the N60 SDS micelle is calculated to be 1.97 ± 0.04 nm which is in a very good agreement with the previous MD studies (1.94 ± 0.04 nm [13]) and only slightly lower than the hydrodynamic radius of 2.2 nm measured by quasi-elastic light scattering spectroscopy [9]. The COM to Nitrogen radius of the DTAC micelle was found to be 1.84 ± 0.06 nm, only slightly higher than the one of ~1.78 nm estimated from NMR measurements [1] and time resolved fluorescence quenching[7], but within the error boundaries.

Table 3. Motional and order parameters of 5DSA ,SDS and DTAC in N60 SDS and N40 DTAC micelles obtained from the fitting of the relevant autocorrelation functions.

T (K)		D^G (s^{-1})	$D_\perp^L$ (s^{-1})	$D_\parallel^L$ (s^{-1})	S^L [a]		D^G (s^{-1})	$D_\perp^L$ (s^{-1})	$D_\parallel^L$ (s^{-1})	S^L [a]
		SDS Micelle					DTAC Micelle			
300	5DSA	3.8 ×10^7	1.26 ×10^8	1.68 ×10^8	0.36	5DSA	5.7 ×10^7	1.39 ×10^8	3.71 ×10^8	0.47
300	SDS	6.9 ×10^7	3.24 ×10^8	9.55 ×10^9	0.55	DTAC	10.1 ×10^7	8.73 ×10^8	10.96×10^9	0.54
310	5DSA	4.6 ×10^7	1.79 ×10^8	3.58 ×10^8	0.35	5DSA	7.4 ×10^7	2.11 ×10^8	4.52 ×10^8	0.44
310	SDS	8.7 ×10^7	5.56 ×10^8	11.61 ×10^9	0.51	DTAC	14.3 ×10^7	12.97 ×10^8	17.42 ×10^9	0.53
320	5DSA	6.7 ×10^7	2.14×10^8	5.45 ×10^8	0.34	5DSA	9.1 ×10^7	2.75 ×10^8	5.67 ×10^8	0.40
320	SDS	10.6 ×10^7	7.37 ×10^8	19.25 ×10^9	0.46	DTAC	19.9 ×10^7	15.15 ×10^8	20.45 ×10^9	0.51

[a] D^G , $D_\perp^L$, $D_\parallel^L$ and S^L represent isotropic global diffusion, the two components of local diffusion and the local order parameter, respectively. 95% confidence bounds for the adjusted parameters are provided in Table S3 of the SI.

In order to evaluate the changes in the shape of the micelles over time, eccentricity parameter, e , defined as:

$$e = 1 - \frac{I_{Min}}{I_{Avg}} \quad (14)$$

was calculated at each time point over the lengths of MD trajectories (Figure S1b of SI). In (14) I_{Min} and I_{Avg} are the smallest and averaged moments of inertia along the principal axes respectively [75] . An eccentricity of 0 indicates a perfect sphere. The averaged over time eccentricity of the SDS micelle was 0.118 ± 0.035, which falls within the range of previously reported values obtained from MD simulations (0.057 [10] - 0.154 [11]). Experimentally, the shape of the SDS micelle is still a topic of debate, with scattering data consistent with both slightly prolate and oblate spheroids [76]. The average eccentricity of the DTAC micelle was found to be slightly higher at 0.163 ± 0.050, with greater fluctuations over the course of the trajectory due to the temporary dissociation and smaller aggregation number (blue line in Figure S1b of SI).

Cross-correlation functions for the *Z* axes of host molecules, calculated via (15):

$$C(t) = \left\langle \frac{1}{2N} \sum_{i \neq j}^{N} P_2(\vec{Z}_i(t+\tau)) \cdot \vec{Z}_j((t)) d\tau \right\rangle \quad (15)$$

where $\vec{Z}_i$ and $\vec{Z}_j$ represent the Z vectors of pairs i and j , respectively, of the hosts are shown in Figure 4b for both SDS and DTAC systems. They indicate that in both cases relatively fast molecular surface diffusion occurs, leading to the loss of coordinated motions among them on the scale of a few nanoseconds. This is also evident in the snapshots shown in Figure 4c where the selected molecules become completely dispersed throughout the micelle after ~10 ns.

These observations have several implications for the dynamics that would not be evident from EPR spectra alone. Firstly, as the micelle radii and eccentricity are in good agreement with those observed in previous studies with micelles free of spin probes, the effect of the probe on the geometry is minimal, even though the formation of micro-aggregates indicates that it acts as a nucleation site. Secondly, because of fluctuating eccentricity of

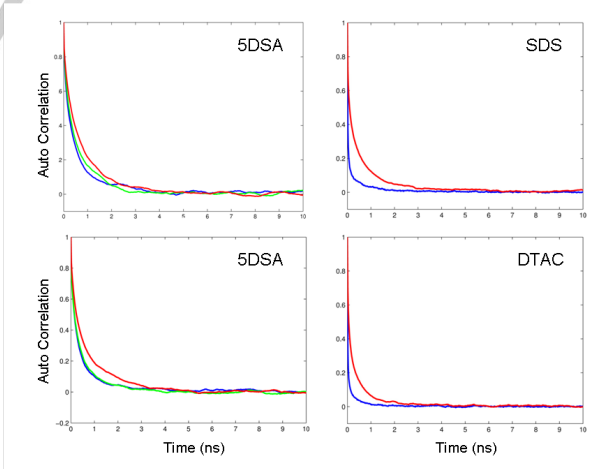

Figure 5. Left: Rotational autocorrelation functions of the magnetic axes *X* (blue), *Y* (green) and *Z* (red) of 5DSA spin probe in SDS (top) and DTAC (bottom) micelles at 320K. Right: Rotational autocorrelation functions of SDS molecular axes of *X, Y* (blue) and *Z* (red) of SDS (top) and DTAC (bottom) surfactants.

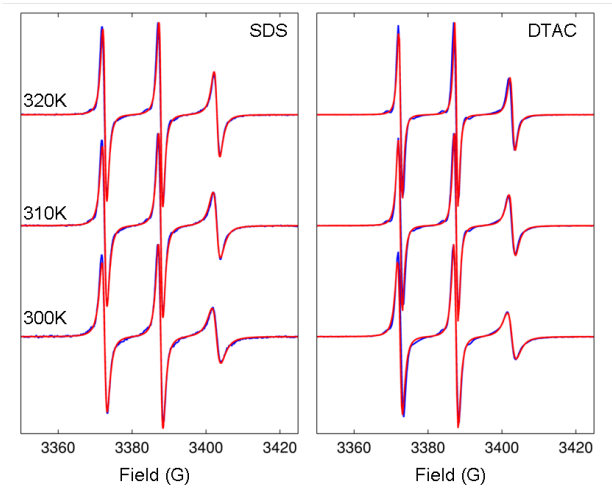

Figure 6. Comparison between experimental (blue) and predicted (red) EPR spectra of SDS (left panel) and DTAC (right panel) micelles doped with 5DSA at selected temperatures.

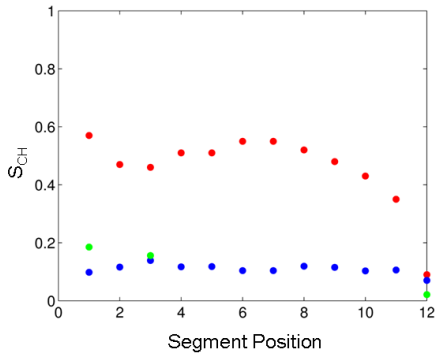

Figure 7. Comparison between experimentally determined (blue[78] and green [79]) and predicted from MD (red) $S_{C\text{-}H}$ order parameters as a function of position along the carbonyl chain in micellar SDS at 310K. Full details are presented in Table S4 of SI.

micelles, global tumbling of the micelle is poorly defined [2, 77]. Furthermore, since surface diffusion of the host molecules is comparatively fast and stochastic, collective motions rapidly fade away as evident in Figure 4b and c.

As a result, the effect of aggregate tumbling on the global motion will be very small for these systems. This suggests that the additional contributions of slippage in the SRLS model are probably not required to describe the motion of the probe in these particular systems, and therefore a simpler model such as the MF approach, can be applied adequately. Additionally, in both systems the nitroxide head group of 5DSA is located at the fully solvent exposed surface, thus the spectra are indicative of only one environment.

The autocorrelation plots of the magnetic and molecular axes of the probe and host molecules, respectively, in micelle aggregation are presented in Figure 5 and were fitted using MF expression S2 from SI. In each case, the decay curves are consistent with the overall axial dynamics which are clearly of bi-exponential character, representing the superposition of fast restricted internal and unrestricted global motions. Table 3 presents the principle rotational diffusion rates and the local order parameters extracted from the fitting of the autocorrelation functions. These parameters indicate the differences between the SDS and DTAC micelles motions that are consistent with their structural features. The larger but structurally disordered SDS micelle shows lower local order for both 5DSA and SDS molecules with slower global motions, whereas in contrast the smaller DTAC micelle shows higher local order for both molecules but with much faster global motional contribution. As smaller micelles have greater curvature of the surface, the effect of surface diffusion on the rotational global motion is higher in the case of DTAC. This result is also consistent with the relative rates observed in the cross-correlations (Figure 4b).

The EPR spectra, shown in Figure 6 in red, were simulated using the parameters given in Table 3 and are in excellent agreement with the experimental ones shown in blue. It is worth noting that even using multiple probes, relatively long trajectories compared with the micro-aggregates were required to adequately resolve the slower global dynamics for the micellar phase. The order parameter (S^L = 0.47) and global dynamics (D^G = 5.7 ×10^7 s^{-1}) calculated for the probe in the DTAC micelle at 300K are both in good agreement with the ones reported by Lindblom and co-workers (S^L = 0.5 and D^G = 3.88 ×10^7 s^{-1} at 298K) [4].

For the SDS micelle, the order parameter was found to be only slightly lower (S^L = 0.36 and D^G = 3.8 ×10^7 s^{-1} at 300K) than that of Westlund and co-workers who fitted the EPR spectra with the two-dynamic model (S^L = 0.43 and D^G = 5.0 ×10^7 s^{-1} at 298K) [3]. Similar to micro-aggregates, the dynamics of the probe was found to be slower than that of the host in all micellar cases, as well as showing lower ordering.

We note that although the calculated from MD values of the segmental order parameter of C-H bonds at different parts of the SDS tail show qualitative agreement with those obtained from NMR relaxation measurements, they are overestimated by approximately a factor of 2.5 as one can see in Figure 7. Although there is some variation in the literature values for C-H order parameters, GAFF, for instance, is known to produce overly ordered alkyl chains in lipid bilayers [80]. These discrepancies have mainly been attributed to an under-representation of *gauche* conformers resulting in stiffened alkane chains [82, 83]. It is interesting to note that recent modelling studies on non-ionic chromonic liquid crystals have confirmed that GAFF also overestimates the interaction between the hydrophilic ethyleneoxy chains of the molecules resulting in their aggregation into compact disorganized clusters instead of ordered stacks [81].

This fact however does not affect the simulated EPR line shapes that demonstrate perfect agreement with experiment at different temperatures. This is because in micellar aggregates the nitroxide group of 5DSA remains fully water exposed throughout the MD runs thus being relatively insensitive to the packing of

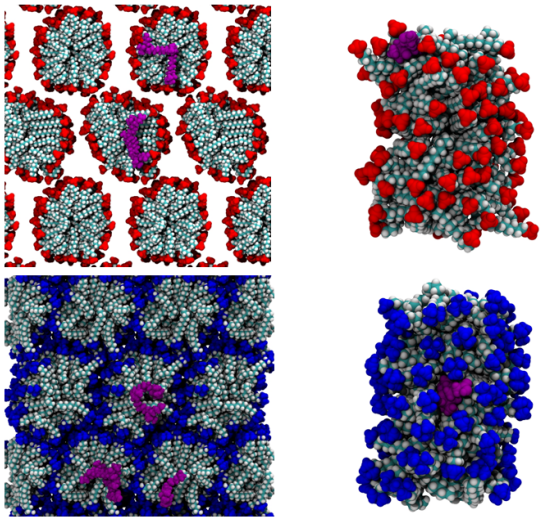

Figure 8. Equilibrated structures of SDS (top) and DTAC (bottom) in hexagonal phases at 320K doped with 5DSA spin probe (purple). In all images water molecules are excluded for clarity.

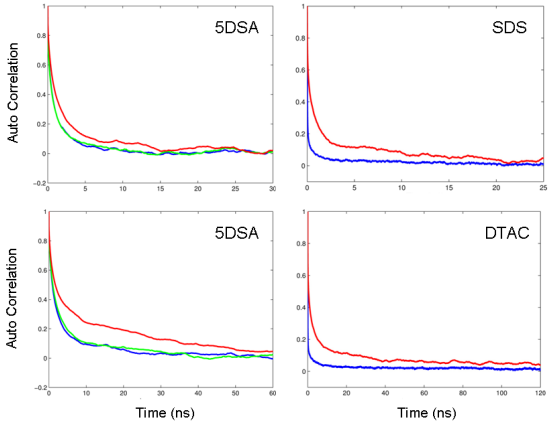

Figure 9. Left: Rotational autocorrelation functions of the magnetic axes *X* (blue), *Y* (green) and *Z* (red) of 5DSA spin probe in SDS (top) and DTAC (bottom) hexagonal phases at 320K. Right: Rotational autocorrelation functions of molecular axes *X, Y* (blue) and *Z* axis (red) of SDS (top) and DTAC (bottom) surfactants.

internal carbonyl chains of the host molecules overestimated by the GAFF model. Importantly, the agreement between the predicted and experimental EPR spectra conclude the validity of the MF approach for the micellar systems.

Hexagonal Phase – Figure 8 presents the snapshots of equilibrated structures of SDS (top) and DTAC (bottom) hexagonal phases doped with 5DSA spin probe (purple) at 320K demonstrating significant geometric differences between the two aggregates. The water content was 50% wt and 30% wt in the SDS and DTAC systems, respectively. The lateral sizes of the simulation boxes were 3.9 nm and 4.7 nm for the SDS and DTAC phases, respectively, with the rods connected by periodic boundary conditions. SDS hexagonal phases form at a lower concentration but higher temperatures compared to DTAC [15, 16]. The higher water content leads to the deviation of SDS from a circular to an elliptical cross section. This result is consistent with scattering and NMR studies [2] and other reports on the elliptical profile for rod-like micelles [84]. On the other hand, a close contact among the rods in DTAC forces the individual rods into having a hexagonal profile, in agreement with the previous studies [12].

Our MD simulations confirmed that at high concentration of water DTAC rods become unstable. For instance, an MD simulation on a single rod with 50% wt resulted in its rapid decomposition into irregular micelles at times < 5 ns. This is consistent with other MD studies of single DTAC [85] and CTAC [86] rods. Conversely the SDS hexagonal phase was more sensitive to temperature, with the molecules rapidly clustering at temperatures below 320K, followed by the growth of crystal patches, eventually leading to a lamellar like ribbon structure [13] (Figure S2 of SI). Although the experimentally determined phase diagram [15] indicates that this temperature is near the phase boundary for a combined hexagonal and crystal region, the phase transition in MD appears particularly rapid, precluding measurement of comparable correlation functions. This might be related to the overly ordered alkyl chains suggested by the high C-H order parameters of the host molecules observed for the micellar phase.

The autocorrelation plots for both the spin probe and the host molecule (Figure 9) clearly indicate a bi-modal dynamics which can be fitted using expression S3 from SI derived for a superposition of local restrained axial dynamics and global axial rotational diffusion of the rod with the main axis of local and global motions being perpendicular to each other. In the case of DTAC both the probe and the host show higher local order compared to SDS, reflecting the more ordered packing in DTAC, but this time with slower global motions which is particularly evident for the host liquid crystal. SDS shows slightly higher order than in the micelle at the same temperature, evident from both the correlation plot and the more regular arrangement of the hydrophobic tails visible in the geometric snapshots. This difference in packing also potentially influences the observed global motion rate where the disordered SDS rods allow for a faster diffusion along the aggregate Z axis than in DTAC.

A slow transverse global motional tumbling ($D_{\perp}^{G}$) of the rods was required in both systems for adequate fits. As has been shown previously such motional contributions are too slow on the X-band EPR timescale and do not affect the EPR line shape [4]. The motional and order parameters obtained from the fitting of autocorrelation functions are summarised in Table 4. The adjusted order parameter for the alkyl chain of SDS has similar value to the ones corresponding to the micellar phase at 320K. The order parameter for DTAC hosts was found to be higher

Table 4. Motional and order parameters of 5DSA, SDS and DTAC in hexagonal phases obtained from the fitting of the relevant autocorrelation functions at 320K.

	$D_{\perp}^{G}$ (s^{-1})	$D_{\parallel}^{G}$ (s^{-1})	$D_{\perp}^{L}$ (s^{-1})	$D_{\parallel}^{L}$ (s^{-1})	S^{L} [a]
			SDS Hexagonal Phase		
5DSA	1.0×10^{6}	5.91×10^{7}	1.15×10^{8}	2.08×10^{8}	0.43
SDS	1.0×10^{6}	6.27×10^{7}	3.75×10^{8}	11.19×10^{9}	0.50
			DTAC Hexagonal Phase		
5DSA	1.0×10^{6}	2.7×10^{7}	0.99×10^{8}	1.11×10^{8}	0.58
DTAC	1.0×10^{6}	3.60×10^{7}	2.73×10^{8}	10.16×10^{9}	0.61

[a] $D_{\perp}^{G}$ $D_{\parallel}^{G}$, $D_{\perp}^{L}$ $D_{\parallel}^{L}$ and S^{L} represent the two components of global diffusion, the two components of local diffusion and the local order parameter, respectively. 95% confidence bounds for the adjusted parameters are provided in Table S5 of the SI.

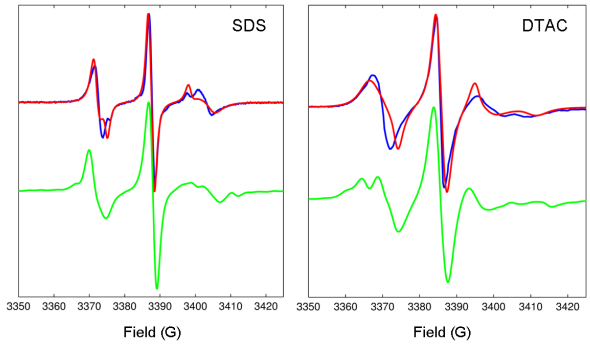

Figure 10. Comparison between experimental (blue) and predicted from MD (red) EPR spectra of SDS (left panel) and DTAC (right panel) hexagonal phases doped with 5DSA spin probe at 320K. Experimental EPR spectrum of DTAC is reproduced from [3] with permission from American Chemical Society. In each panel green lines represent the EPR line shapes predicted directly and completely from MD trajectories using the propagation approach.

than in the corresponding micellar phase, due to the tighter packing of the rods, in agreement with the trend reported previously [4].

Comparison between the predicted EPR spectra of SDS and DTAC hexagonal phases at 320K (red lines) and experimental ones (blue lines) are shown in Figure 10, demonstrating reasonably good agreement between them. In particular, because of the overall slower and more restrained dynamics of the probe in DTAC the simulated EPR spectra of DTAC are broader compared to SDS, in agreement with experiment. Similar to micelles, in both systems the nitroxide head group of 5DSA remains located at the aggregate surface throughout the MD simulations. As a result, the dynamics of the nitroxide group of the probe in both SDS and DTAC is predetermined by the interaction with the water molecules with relatively minor effect from the overly ordered dynamics of the alkyl chains. Some discrepancies observed between simulated and experimental EPR line shapes can be attributed to the simplicity of the simulation model employed. Previous studies have noted a number of defects [2] that could exist in rod like aggregates but not be properly replicated in MD. The periodic boundaries used in MD runs imply rods of effectively infinite length. In fact, they are finite in length and their spherocylinder ends will provide a different contribution to the EPR spectra. The periodic nature of the rods also prevents 'worm' like distortions which could be significant in the SDS aggregates where the higher water content may allow their bending [3]. Temporary bulges were also observed in the SDS rods which could cause additional rotational contributions.

In order to check the validity of the MF approach in the simulation of EPR spectra we have also performed simulation of the spectra directly and completely from MD trajectories using the MD-EPR propagation simulation method developed previously [23, 47, 48, 50] (for details see Supporting Information).

Significantly longer MD trajectories were required for an adequate simulation by the direct propagation method (see Table 1). Analysis clearly demonstrated the sensitivity of the simulated line shapes to their lengths. The resulting EPR spectra are shown in Figure 10 as green lines for both SDS and DTAC demonstrating reasonably good agreement with both the experimental spectra and the ones predicted using the MF approach confirming the validity of the latter.

Lamellar Phase – Equilibrated structures of lamellar phases of SDS (top) and DTAC (bottom) at 350K doped with 5DSA spin probes are shown in Figure 11. In both cases, because of the very low water content (30% wt in SDS and 10% wt in DTAC), two lamellae were used in all MD simulations in order to prevent direct interaction of the bilayer with its image in the simulation box. Considerable structural differences were observed between the lamellar phases of the two surfactants, with SDS showing a more prominent curvature of the surface resulting from the higher water content. Due to close molecular packing, repulsion between head groups of SDS causes a vertical translational motion. As a result the molecules remain well aligned over these ripples. Because of the efficient packing of the molecules, the lamellae thickness of ~1.9 nm, calculated as the distance from sulphur to sulphur, exceeds only slightly the all-trans molecular length of ~ 1.68 nm, calculated as the distance between terminal carbon to sulphur. When the thickness of the water layer is included, the approximate value of the unit cell length calculated from MD (3.3 nm) is in perfect agreement with the one measured experimentally using neutron scattering (~3.3 nm) [15]. The calculated area per head group in SDS (0.40 nm^2 (Figure S3 of SI)) also shows perfect agreement with the experimentally determined one using X-ray scattering (0.40 nm^2) [87] and indicates that the structure is stable over the entire MD production run. In order to check the size consistency of the simulated models additional MD simulations have been

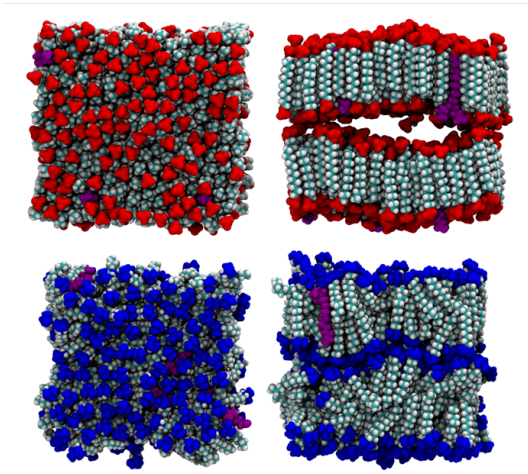

Figure 11. Equilibrated structures of SDS (top) and DTAC (bottom) in lamellar phases at 350K doped with 5DSA spin probe (purple). In all images water molecules are excluded for clarity.

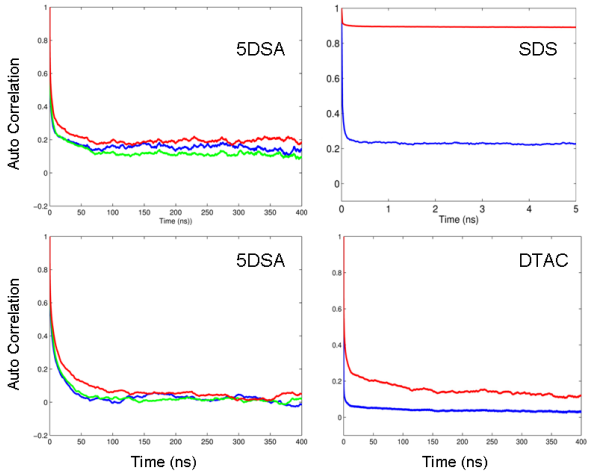

Figure 12. Left: Rotational autocorrelation functions of the magnetic axes *X* (blue), *Y* (green) and *Z* (red) of 5DSA spin probe in SDS (top) and DTAC (bottom) in the lamellar phase at 350K. Right: Rotational autocorrelation functions of molecular axes *X*, *Y* (blue) and *Z* axis (red) of SDS (top) and DTAC (bottom) surfactants.

performed for extended systems (3 lamellae in the larger simulation box) for both SDS and DTAC. The values of the calculated geometric parameters, namely, the area per head group and thickness were totally consistent with the ones obtained with 2 lamellae in the box although sufficiently longer simulation times were required.

The backbones of the probes remain located in the interior of the SDS lamellae, with the head groups exposed to water at the surface.

Table 5. Motional and order parameters of 5DSA, SDS and DTAC in lamellar phases obtained from the fitting of the relevant autocorrelation functions at 350K.

	$D_{\perp}^{G}$ (s^{-1})	S^{G}	$D_{\perp}^{L}$ (s^{-1})	S^{L} [a]	S^{Eff}	$D_{\parallel}^{Eff}$ (s^{-1}) [b]
			SDS Lamellar Phase			
5DSA	3.57×10^{6}	0.74	1.19×10^{8}	0.59	0.44	1.7×10^{6}
SDS	1.17×10^{7}	0.99	2.82×10^{8}	0.95	0.95	10.5×10^{9}
			DTAC Lamellar Phase			
5DSA	4.69×10^{6}	0.38	9.34×10^{7}	0.68	0.24	1.3×10^{7}
DTAC	1.01×10^{6}	0.69	9.29×10^{7}	0.51	0.36	12.5×10^{9}

[a] $D_{\perp}^{G}$, S^{G} and $D_{\perp}^{L}$, S^{L} represent relevant rotation diffusion components and order parameters of global and local motions, respectively. 95% confidence bounds for the adjusted parameters are provided in Table S6 of the SI.

[b] $D_{\parallel}^{Eff}$ is the effective axial diffusion rate defined as: $D_{\parallel}^{Eff} = D_{\parallel}^{G} + D_{\parallel}^{L}$ (see equation S4 from SI).

In contrast, in the DTAC lamellar phase, although there is less surface curvature, the interior appears to be more disordered compared to the SDS case, as seen in Figure 11. The area per molecule (0.45 nm^2), shown as the blue line in Figure S3 of SI, is characterised by significantly wider fluctuations compared to the SDS lamellae, again being consistent with a more disordered structure, although experimental data for this is not available for comparison. It is interesting to note that during the simulation we even were able to observe the formation of a narrow pore in DTAC lamellae (shown in Figure S4 of SI) with small degree of water penetration, both attributed to the high level of disorder in acyl chains. The packing arrangement was similar to that observed commonly for lipid bilayers, with upper and lower leaflets, resulting in a thickness of ~ 2.2 nm calculated as the distance between head nitrogens. This is significantly greater than that of the all-trans molecular length of 1.54 nm calculated between the terminal carbon and nitrogen. Because of the thinner water layer in DTAC the two lamellae are in close contact with each other allowing the probe to drift between them as shown in Figure S5 of SI. As a result 5DSA in DTAC experiences a significantly different environment to that of SDS lamellae and other phases with the nitroxide group penetrating deep into the hydrophobic interior. This is confirmed by the calculated radial distribution functions shown in Figure S6 of SI where the average distance between the mid alkyl carbon on the host molecule and the nitroxide head group of the probe is found

to be approximately twice as low as in the DTAC lamellae (0.6 nm) compared with the SDS lamellae (1.1 nm).

Because of slow global motions of the probe in these phases, long trajectories were required to resolve the dynamics and extract the motional and order parameters from the autocorrelation plots, even with multiple probes employed. The autocorrelation functions for the probes and host molecules in lamellae phases are shown in Figure 12. Dynamical and order parameters obtained from the fitting of the autocorrelation functions using the relevant equation S4 from SI are summarized in Table 5. In particular, for the SDS lamellae the global motional component is highly restrained for both 5DSA and SDS molecules. Also, there is a significant difference in the ordering between the probe and the host molecules in the SDS system resulting in a much higher effective order parameter $S^{Eff} = S^G S^L$ observed for the host compared to the probe. This is attributed to a more flexible position of the nitroxide head group at the surface. In contrast, in the DTAC lamellae phase both 5DSA and DTAC molecules are able to tilt during the motions resulting in significantly reduced effective order parameter for both.

The apparent ratio between the order parameters for the *X/Y* and *Z* axes of the liquid crystal hosts in both SDS and DTAC lamellae are consistent with the one predicted from the associated MF expression S4 of SI, namely, $(S_{XY}^{Eff}/S_Z^{Eff})^2 = 1/4$. The same ratio is observed for 5DSA, although the effect from the limited number of 5DSA spin probes employed resulted in wider statistical fluctuations in the correlation functions at longer times, making this ratio less apparent, particularly in the case of DTAC lamellae.

Comparison between spectra predicted from MD using the MF approach and experimental EPR spectra for SDS and DTAC lamellae phases is shown in Figure 13. A reasonably good agreement is observed between the simulated and experimental spectra in the case of SDS lamellae shown in Figure 13 (left) as red and blue lines, respectively. Note that the value of homogeneous line broadening used in this case was taken from [3] without further adjustment. The situation is principally different for DTAC lamellae where there is a clear disagreement between the predicted and experimental spectra. The simulated EPR line shape represented in Figure 13 (right) by the red line is significantly broader compared to the experimental one (blue line). In order to check the validity of the MF based simulation approach, EPR spectra were also simulated directly from MD trajectories using the propagation approach and are presented for comparison in Figure 13 as green lines for both SDS and DTAC lamellae. As in the case of hexagonal phases, significantly longer MD trajectories were required (~ 900 ns) for this method. In both cases, for SDS and DTAC, the line shapes predicted directly from MD trajectories are broadly in agreement with the ones predicted by employing SLE in the F-P form with the simulation parameters extracted from MD data using the MF approach. Therefore, the MF approach remains valid in the case of the lamellar phase. The disagreement of the simulated EPR line shapes with the experimental ones for DTAC is attributed to the fact that the nitroxide head group of the probe in the DTAC lamellar phase, contrary to other DTAC phases and also SDS

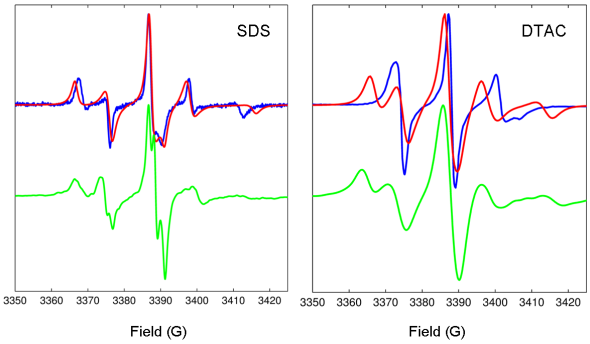

Figure 13. Comparison between experimental (blue) and predicted from MD (red) EPR spectra of SDS (left panel) and DTAC (right panel) lamellae phases doped with 5DSA at 350K. Experimental EPR spectrum of DTAC is reproduced from [3] with permission from American Chemical Society. In each panel the green lines represent the EPR line shapes predicted directly and completely from MD trajectories using the propagation approach.

lamellae, spends a significant amount of time within the environment of the acyl carbon chains. As a result, the packing of the carbon chains, which is overestimated by the GAFF model, also increases the order of the probe, resulting in the broadening of the respective EPR spectra. This effect is less pronounced in the case of SDS lamellae where the nitroxide head group remains positioned predominantly at the surface-water interface.

Conclusions

This study reports the first simulation of CW EPR spectra of lyotropic liquid crystals at different aggregate states from the results of MD modelling. The simulations have been achieved by solving the SLE in the F-P that employs the rotational diffusional operator describing stochastic motion of the probe. The parameters describing such motion in different lyotropic aggregates are extracted from MD trajectories using the MF approach. The purpose of this work was two-fold. Firstly, simulation of EPR line shapes from the results of MD modelling and comparing them to experiment provided an ultimate test bed for the force fields currently employed to model such systems. Secondly, and of equal importance, such a combined MD-EPR methodology allowed us to test the validity of the application of the MF approach that is widely used to interpret spectroscopic data. Our results demonstrated perfect agreement between predicted and experimental EPR spectra for both micro-aggregate and micellar phases of SDS and DTAC liquid crystals. A good agreement has been achieved for hexagonal phases of SDS and DTAC and also for the lamellae phase of SDS. In hexagonal and lamellae phases of both SDS and DTAC EPR simulations using the MF approach were broadly in agreement with the simulations of the EPR spectra from MD trajectories using the direct propagation approach reported by us previously thus confirming the validity of the MF approach for the reported systems. For hexagonal phases some discrepancies observed in the EPR spectra simulated by both SLE-FP and propagation methods were attributed to additional effects, e.g. 'worm' like distortions and finite rod shapes, not accounted for in the MD

simulation model. The disagreement between the simulated and experimental EPR spectra for the DTAC lamellar phase is attributed to the overestimation by GAFF of the packing and order of the carbon acyl chains of the host lyotropics. In DTAC lamellae the nitroxide head group of the probe penetrates deep inside the environment of the carbon chains, resulting in its increased motional restraint and consequent broadening of the EPR spectrum.

Finally, it is important to note that simulation parameters estimated by the fitting of autocorrelation curves generated from MD trajectories using the MF approach usually require much shorter trajectory lengths compared to the ones used in the direct propagation methods. Thus, in many cases EPR simulations from MD autocorrelation functions combined with the MF approach would be advantageous compared to direct propagation techniques.

Acknowledgements

VSO gratefully acknowledges financial support of this work from EPSRC (grants EP/H020411/1 and EP/L001322/1). The authors wish to thank the Research Computing Service at the University of East Anglia for access to the High Performance Computing Cluster (Grace).

Keywords: lyotropic liquid crystals • MD simulations • Electron Paramagnetic Resonance (EPR) • molecular dynamics • spin probe

[1] O. Soederman, H. Walderhaug, U. Henriksson, P. Stilbs, *J. Phys. Chem.* **1985**, *89*, 3693-3701.
[2] P. O. Quist, B. Halle, I. Furó, *J. Chem. Phys.* **1991**, *95*, 6945-6961.
[3] Z. Liang, G. Wikander, P. O. Westlund, *J. Chem. Phys.* **1995**, *102*, 1471-1480.
[4] G. Wikander, P. O. Eriksson, E. E. Burnell, G. Lindblom, *J. Phys. Chem.* **1990**, *94*, 5964-5972.
[5] M. A. Bahri, M. Hoebeke, A. Grammenos, L. Delanaye, N. Vandewalle, A. Seret, *Colloids and Surf., A* **2006**, *290*, 206-212.
[6] B. L. Bales, L. Messina, A. Vidal, M. Peric, O. R. Nascimento, *J. Phys. Chem. B* **1998**, *102*, 10347-10358.
[7] L. B. A. Johansson, O. Soederman, *J. Phys. Chem.* **1987**, *91*, 5275-5278.
[8] F. Reiss-Husson, V. Luzzati, *J. Phys. Chem.* **1964**, *68*, 3504-3511.
[9] N. A. Mazer, G. B. Benedek, M. C. Carey, *J. Phys. Chem.* **1976**, *80*, 1075-1085.
[10] B. J. Chun, J. I. Choi, S. S. Jang, *Colloids Surf. A* **2015**, *474*, 36-43.
[11] F. Palazzesi, M. Calvaresi, F. Zerbetto, *Soft Matter* **2011**, *7*, 9148-9156.
[12] V. Kocherbitov, *J. Mol. Liq.* **2015**, *210*, 74-81.
[13] X. Tang, P. H. Koenig, R. G. Larson, *J. Phys. Chem. B* **2014**, *118*, 3864-3880.
[14] C. D. Bruce, M. L. Berkowitz, L. Perera, M. D. E. Forbes, *J. Phys. Chem. B* **2002**, *106*, 3788-3793.
[15] P. Kekicheff, B. Cabane, *Acta Crystallogr., Sect. B* **1988**, *44*, 395-406.
[16] R. R. Balmbra, J. S. Clunie, J. F. Goodman, *Nature* **1969**, *222*, 1159-1160.
[17] A. Nayeem, J. H. Freed, *J. Phys. Chem.* **1989**, *93*, 6539-6550.
[18] H. Gopee, A. N. Cammidge, V. S. Oganesyan, *Angew. Chem. Int. Ed.* **2013**, *52*, 8917-8920.
[19] C. Bacchiocchi, I. Miglioli, A. Arcioni, I. Vecchi, K. Rai, A. Fontecchio, C. Zannoni, *J. Phys. Chem. B* **2009**, *113*, 5391-5402.
[20] G. R. Luckhurst, M. Setaka, C. Zannoni, *Mol. Phys.* **1974**, *28*, 49-68.
[21] C. Zannoni, G. F. Pedulli, L. Masotti, A. Spisni, *J. Mag. Reson.* **1981**, *43*, 141-153.
[22] S. K. Misra, J. H. Freed, in *Multifrequency Electron Paramagnetic Resonance* (Ed.: S. K. Misra), Wiley-VCH Verlag GmbH & Co. KGaA, Weinheim, Germany, **2011**, pp. 497-544.
[23] V. S. Oganesyan, in *SPR: Electron Paramagnetic Resonance, Vol. 24* (Eds.: B. C. Gilbert, V. Chechik., D. M. Murphy), The Royal Society of Chemistry, London, **2015**, pp. 32-61.
[24] J. H. Freed, G. V. Bruno, C. F. Polnaszek, *J. Phys. Chem.* **1971**, *75*, 3385-3399.
[25] C. F. Polnaszek, G. V. Bruno, J. H. Freed, *J. Chem. Phys.* **1973**, *58*, 3185-3199.
[26] S. Stoll, A. Schweiger, *J. Mag. Reson.* **2006**, *178*, 42-55.
[27] D. J. Schneider, J. H. Freed, in *Spin Labeling: Theory and Applications* (Eds.: L. J. Berliner, J. Reuben), Springer US, Boston, MA, **1989**, pp. 1-76.
[28] D. D. Lasic, H. Hauser, *J. Phys. Chem.* **1985**, *89*, 2648-2651.
[29] A. Polimeno, J. H. Freed, *J. Phys. Chem.* **1995**, *99*, 10995-11006.
[30] V. A. Livshits, D. Kurad, D. Marsh, *J. Mag. Reson.* **2006**, *180*, 63-71.
[31] Y. Lou, M. Ge, J. H. Freed, *J. Phys. Chem. B* **2001**, *105*, 11053-11056.
[32] Z. Liang, Y. Lou, J. H. Freed, L. Columbus, W. L. Hubbell, *J. Phys. Chem. B* **2004**, *108*, 17649-17659.
[33] Y. E. Nesmelov, D. D. Thomas, *Biophys. Rev.* **2010**, *2*, 91-99.
[34] Z. Liang, J. H. Freed, R. S. Keyes, A. M. Bobst, *J. Phys. Chem. B* **2000**, *104*, 5372-5381.
[35] Z. Liang, J. H. Freed, *J. Phys. Chem. B* **1999**, *103*, 6384-6396.
[36] G. Lipari, A. Szabo, *J. Am. Chem. Soc.* **1982**, *104*, 4546-4559.
[37] M. J. Knight, A. J. Pell, I. Bertini, I. C. Felli, L. Gonnelli, R. Pierattelli, T. Herrmann, L. Emsley, G. Pintacuda, *Proc. Natl. Acad. Sci. USA* **2012**, *109*, 11095-11100.
[38] B. Liang, A. Arora, L. K. Tamm, *Biochim. Biophys. Acta, Biomembranes* **2010**, *1798*, 68-76.
[39] V. A. Daragan, K. H. Mayo, *J. Mag. Reson., Series B* **1996**, *110*, 164-175.
[40] R. Cole, J. P. Loria, *J. Biomol. NMR* **2003**, *26*, 203-213.
[41] J. M. Bui, J. Gsponer, M. Vendruscolo, C. M. Dobson, *Biophys. J.* **2009**, *97*, 2513-2520.
[42] T. M. Ferreira, O. H. Samuli Ollila, R. Pigliapochi, A. P. Dabkowska, D. Topgaard, *J. Chem. Phys.* **2015**, *142*, 044905.
[43] H.-J. Steinhoff, W. L. Hubbell, *Biophys. J.* **1996**, *71*, 2201-2212.
[44] K. A. Earle, D. E. Budil, in *Advanced ESR Methods in Polymer Research* (Ed.: S. Schlick), John Wiley & Sons, Inc., Hoboken, USA, **2006**, pp. 53-83.
[45] C. Beier, H.-J. Steinhoff, *Biophys. J.* **2006**, *91*, 2647-2664.
[46] D. Sezer, J. H. Freed, B. Roux, *J. Phys. Chem. B* **2008**, *112*, 11014-11027.
[47] S. C. DeSensi, D. P. Rangel, A. H. Beth, T. P. Lybrand, E. J. Hustedt, *Biophys. J.* **2008**, *94*, 3798-3809.
[48] V. S. Oganesyan, *Phys. Chem. Chem. Phys.* **2011**, *13*, 4724-4737.
[49] D. Sezer, J. H. Freed, B. Roux, *J. Am. Chem. Soc.* **2009**, *131*, 2597-2605.
[50] V. S. Oganesyan, *J. Mag. Reson.* **2007**, *188*, 196-205.
[51] V. S. Oganesyan, F. Chami, G. F. White, A. J. Thomson, *J. Mag. Reson.* **2017**, *274*, 24-35.
[52] E. Kuprusevicius, G. White, V. S. Oganesyan, *Faraday Discuss.* **2011**, *148*, 283-298.
[53] G. Tiberio, L. Muccioli, R. Berardi, C. Zannoni, *Chem. Phys. Chem.* **2009**, *10*, 125-136.
[54] C. Bacchiocchi, I. Miglioli, A. Arcioni, K. Rai, A. Fontecchio, C. Zannoni, *Mol. Cryst. Liq. Cryst.* **2012**, *558*, 127-139.

[55] E. Kuprusevicius, R. Edge, H. Gopee, A. N. Cammidge, E. J. L. McInnes, M. R. Wilson, V. S. Oganesyan, *Chem. Eur. J.* **2010**, *16*, 11558-11562.
[56] V. S. Oganesyan, E. Kuprusevicius, H. Gopee, A. N. Cammidge, M. R. Wilson, *Phys. Rev. Lett.* **2009**, *102*, 013005.
[57] F. Chami, M. R. Wilson, V. S. Oganesyan, *Soft Matter* **2012**, *8*, 6823-6833.
[58] G. W. T. M. J. Frisch, H. B. Schlegel, G. E. Scuseria, M. A. Robb, J. R. Cheeseman, G. Scalmani, V. Barone, G. A. Petersson, H. Nakatsuji, X. Li, M. Caricato, A. Marenich, J. Bloino, B. G. Janesko, R. Gomperts, B. Mennucci, H. P. Hratchian, J. V. Ortiz, A. F. Izmaylov, J. L. Sonnenberg, D. Williams-Young, F. Ding, F. Lipparini, F. Egidi, J. Goings, B. Peng, A. Petrone, T. Henderson, D. Ranasinghe, V. G. Zakrzewski, J. Gao, N. Rega, G. Zheng, W. Liang, M. Hada, M. Ehara, K. Toyota, R. Fukuda, J. Hasegawa, M. Ishida, T. Nakajima, Y. Honda, O. Kitao, H. Nakai, T. Vreven, K. Throssell, J. A. Montgomery, Jr., J. E. Peralta, F. Ogliaro, M. Bearpark, J. J. Heyd, E. Brothers, K. N. Kudin, V. N. Staroverov, T. Keith, R. Kobayashi, J. Normand, K. Raghavachari, A. Rendell, J. C. Burant, S. S. Iyengar, J. Tomasi, M. Cossi, J. M. Millam, M. Klene, C. Adamo, R. Cammi, J. W. Ochterski, R. L. Martin, K. Morokuma, O. Farkas, J. B. Foresman, and D. J. Fox, Gaussian, Inc., Wallingford CT,, **2009**.
[59] C. M. Breneman, K. B. Wiberg, *J. Comp. Chem.* **1990**, *11*, 361-373.
[60] W. D. Cornell, P. Cieplak, C. I. Bayly, I. R. Gould, K. M. Merz, D. M. Ferguson, D. C. Spellmeyer, T. Fox, J. W. Caldwell, P. A. Kollman, *J. Am. Chem. Soc.* **1995**, *117*, 5179-5197.
[61] V. Barone, A. Bencini, M. Cossi, A. D. Matteo, M. Mattesini, F. Totti, *J. Am. Chem. Soc.* **1998**, *120*, 7069-7078.
[62] L. Martínez, R. Andrade, E. G. Birgin, J. M. Martínez, *J. Comp. Chem.* **2009**, *30*, 2157-2164.
[63] J. Wang, R. M. Wolf, J. W. Caldwell, P. A. Kollman, D. A. Case, *J. Comp. Chem.* **2004**, *25*, 1157-1174.
[64] H. J. C. Berendsen, J. R. Grigera, T. P. Straatsma, *J. Phys. Chem.* **1987**, *91*, 6269-6271.
[65] I. S. Joung, T. E. Cheatham, *J. Phys. Chem. B* **2008**, *112*, 9020-9041.
[66] D. A. Case, T. A. Darden, T. E. C. III, C. L. Simmerling, J. Wang, R. E. Duke, R. Luo, R. C. Walker, W. Zhang, K. M. Merz, B. Roberts, S. Hayik, A. Roitberg, G. Seabra, J. Swails, A. W. Götz, I. Kolossváry, K. F. Wong, F. Paesani, J. Vanicek, R. M. Wolf, J. Liu, X. Wu, S. R. Brozell, T. Steinbrecher, H. Gohlke, Q. Cai, X. Ye, J. Wang, M. J. Hsieh, G.Cui, D. R. Roe, D. H. Mathews, M. G. Seetin, R. Salomon-Ferrer, C. Sagui, V. Babin, T.Luchko, S. Gusarov, A. Kovalenko, P. A. Kollman, University of California, San Francisco, **2012**.
[67] D. E. Budil, S. Lee, S. Saxena, J. H. Freed, *J. Mag. Reson., Series A* **1996**, *120*, 155-189.
[68] L. J. Schwartz, A. E. Stillman, J. H. Freed, *J. Chem. Phys.* **1982**, *77*, 5410-5425.
[69] R. Kubo, *J. Math. Phys.* **1963**, *4*, 174-183.
[70] M. Zerbetto, A. Polimeno, P. Cimino, V. Barone, *J. Chem. Phys.* **2008**, *128*, 024501.
[71] B. J. Gaffney, H. M. McConnell, *J. Mag. Reson.* **1974**, *16*, 1-28.
[72] N. Usova, L. Persson, P.-O. Westlund, *Phys. Chem. Chem. Phys.* **2000**, *2*, 2785-2793.
[73] E. Meirovitch, A. Nayeem, J. H. Freed, *J. Phys. Chem.* **1984**, *88*, 3454-3465.
[74] M. F. Ottaviani, R. Daddi, M. Brustolon, N. J. Turro, D. A. Tomalia, *Appl. Mag. Reson.* **1997**, *13*, 347-363.
[75] S. Salaniwal, S. T. Cui, H. D. Cochran, P. T. Cummings, *Langmuir* **2001**, *17*, 1773-1783.
[76] S. Vass, J. S. Pedersen, J. Pleštil, P. Laggner, E. Rétfalvi, I. Varga, T. Gilányi, *Langmuir* **2008**, *24*, 408-417.
[77] Z. Liang, P. O. Westlund, G. Wikander, *J. Chem. Phys.* **1993**, *99*, 7098-7107.
[78] J. F. Ellena, R. N. Dominey, D. S. Cafiso, *J. Phys. Chem.* **1987**, *91*, 131-137.
[79] O. Soederman, G. Carlstrom, U. Olsson, T. C. Wong, *J. Chem. Soc., Faraday T. 1* **1988**, *84*, 4475-4486.
[80] C. J. Dickson, L. Rosso, R. M. Betz, R. C. Walker, I. R. Gould, *Soft Matter* **2012**, *8*, 9617-9627.
[81] A. Akinshina, M. Walker, M. R. Wilson, G. J. T. Tiddy, A. J. Masters, P. Carbone, *Soft Matter* **2015**, *11*, 680-691.
[82] N. J. Boyd, M. R. Wilson, *Phys. Chem. Chem. Phys.* **2015**, *17*, 24851-24865.
[83] A. P. Lyubartsev, A. L. Rabinovich, *Soft Matter* **2011**, *7*, 25-39.
[84] M. Bergstrom, J. Skov Pedersen, *Phys. Chem. Chem. Phys.* **1999**, *1*, 4437-4446.
[85] J. Gujt, M. Bešter-Rogač, E. Spohr, *Langmuir* **2016**, *32*, 8275-8286.
[86] Z. Wang, R. G. Larson, *J. Phys. Chem. B* **2009**, *113*, 13697-13710.
[87] M. K. Minasyanc, V. A. Zakaryan, A. A. Shahinyan, I. G. Chistyakov, *Kristallografiya* **1979**, *24*, 319-324.

10.1002/chem.201702682

WILEY-VCH

Entry for the Table of Contents (Please choose one layout)

FULL PAPER

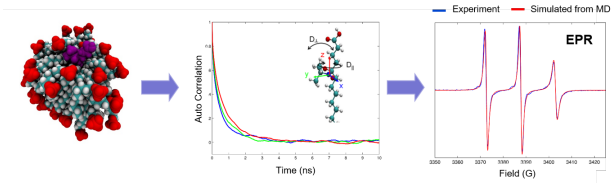

Characterisation of molecular organisation and motions in different aggregate states of lyotropic liquid crystals by a combination of all-atom MD simulations and EPR spectroscopy.

*Christopher Prior, Vasily S. Oganesyan**

Page No. – Page No.

Prediction of EPR spectra of lyotropic liquid crystals using Molecular Dynamics simulations and the Model Free Approach